## METHODS

### Recombinant protein expression and purification

The coding sequences for human RagA (UniProtKB: Q7L523; synthetic gene codon optimized by Life Technologies) and RagC (UniProtKB: Q9HB90; Source BioScience IMAGE:4342448) were PCR amplified and cloned for co-expression in a pOPC polycistronic expression vector (*47*). RagC was cloned with an N-terminal His6 tag followed by a lipoyl domain (*48*) and a TEV cleavage site, while RagA had no tag. PCR products for the inserts were cloned into the plasmid backbone using In-Fusion HD enzyme premix (TaKaRa, 638911). For creating an active Rag heterodimer with RagA in a GTP-locked form and RagC in a GDP-locked form, we constructed relevant mutants of the individual subunits such as RagA-Q66L, RagC-S75N and the cancer-derived mutant RagC-T90N. For the crystallization of Rag heterodimers, the N-terminal region of RagC that HDX-MS suggested was likely to be disordered was truncated. We designed two variants of RagC, RagC-(34-399) and RagC-(40-399). Both were co-expressed with the tagless RagA. An inactive Rag heterodimer with RagA in a GDP-locked form and RagC in a GTP-locked form was constructed, by making a heterodimer with RagA-T21N and RagC-Q120L mutations. Full-length human PRAS40 (UniProtKB: Q96B36; Source BioScience IMAGE:2988648) was PCR amplified and cloned into a pOPTL bacterial expression vector, which has an N-terminal His6-tag followed by a lipoyl domain and a TEV cleavage site. The 'PRAS40-fused-RagA/C' construct where the N-terminus of full-length RagC-T90N was covalently linked to the C-terminus of full-length PRAS40 was produced similarly to the above-mentioned RagA/C constructs using the co-expression vector pOPC with the tagless RagA.

All Rag constructs were expressed in *E. coli* LOBSTR cells (EC1001, KeraFast) in 2xTY media. Cells were grown at 37 °C until the $OD_{600}$ reached 0.7, then expression was induced with 0.5 mM isopropyl-d-1-thiogalactopyranoside for 18 h at 20 °C. Harvested cells

were lysed in a buffer containing 50 mM Tris-HCl pH 8.0, 300 mM NaCl, 10% glycerol (v/v), 0.5 mM TCEP, 10 mM imidazole and two tablets of complete EDTA-free protease cocktail inhibitors (Roche, 05056489001) per 150 mL of cell lysate, and 2 U/mL of Pierce Universal Nuclease (Thermo Fisher Scientific, 88702). The cells were disrupted by sonication for 2 min at 60 % power (Vibra-Cell, Sonics and Materials Inc.) at 4 °C. The whole cell lysate was cleared by centrifugation in a Ti45 rotor at 35000 rpm for 35 min. The cleared supernatant was applied to a 5 ml HisTrap column (GE Healthcare) and eluted with an imidazole gradient. The eluted samples were purified by ion exchange chromatography on a HiTrapQ column and the concentrated protein was then treated with TEV protease overnight at 4 ºC to cleave the N-terminal $His_6$ and lipoyl tags. Prior to size-exclusion chromatography, the sample was loaded with nucleotides as previously described (*49*). In short, heterodimers were incubated with 5 mM EDTA for 60 min, and after addition of $MgCl_2$ to the final concentration of 20 mM, both 5 mM GTP (Jena, NU-1012-IG) and 5 mM GDP (Sigma, G7127) were added and incubated for the final 60 min. The nucleotide-loaded sample was then purified by size-exclusion chromatography on a Superdex 200 16/60 column (GE Healthcare) equilibrated with a mobile buffer consisting of 50 mM HEPES pH 7.5, 150 mM NaCl, 1 mM TCEP and 2 mM $MgCl_2$. Fractions containing Rag GTPases were concentrated using Ultra-4 Ultracel-30K (Millipore, UFC803024) to approximately 20 mg/mL or above, frozen in liquid nitrogen and stored at -80 ºC until further use. The truncated Rag constructs for crystallization were purified in the same way as the full-length Rag heterodimers. RagA-$Q66L_{GTP}$/RagC(34-399)-$T90N_{GDP}$, RagA-$Q66L_{GTP}$/RagC(40-399)-$S75N_{GDP}$ and RagA-$T21N_{GDP}$/RagC(40-399)-$Q120L_{GTP}$ were supplemented with both GTP and GDP during the nucleotide–loading step. The human PRAS40-WT and PRAS40-fused-RagA/C were expressed and purified using the same procedure as described for the RagA/C.

For the production of human mTORC1 complex, the three subunits were PCR amplified from plasmids encoding human RAPTOR (Addgene 8513), human mLST8 (Source BioScience IMAGE:5926090) and human mTOR (Sino Biological Inc.). Each gene was cloned individually into a pCAG mammalian expression vector (modified from Addgene 11160): mTOR and mLST8 without tags and RAPTOR with an N-terminal tag, either 2XStrep-tag II followed by a TEV cleavage site or a 2XStrep-tag II-1XFLAG-tag without a cleavage site. The mTORC1 complex was produced by transient transfection of Expi293F cells (Thermo Fisher A14527) grown in Expi293 media (Thermo Fisher A1435102) in a Multitron Pro shaker set at 37 °C, 8% CO2 and 125 rpm. For the transfections, the three plasmids (total 1.1 mg DNA/L cells) were co-transfected using PEI (Polyethyleneimine "MAX", MW 40,000, Polysciences, 24765, total 3 mg PEI/L cells) into cells at a density of $2.5x10^6$ cells/mL. After 48 h, cells were collected by centrifugation and cell pellets were frozen in liquid $N_2$ and stored at -80 °C. The harvested cells were lysed in 50 mM HEPES, pH 7.5, 200 mM NaCl, 0.4% CHAPS and 1 mM TCEP. After 30 min incubation at 4 ºC, the cell lysate was cleared by centrifugation in a Ti45 rotor at 15000 rpm for 35 min. A 5 mL StrepTrap HP prepacked column (GE Healthcare, 28-9075-48) was first washed with water and equilibrated with wash buffer (50 mM HEPES, pH 7.5, 200 mM NaCl, 0.3% CHAPS, 1 mM TCEP). Cleared supernatant was loaded onto the StrepTrap column. After extensive washing, the Strep-tagged proteins were eluted with a buffer containing 10 mM D-desthiobiotin (IBA, 2-1000-005). For the cryo-EM analysis, instead of eluting with D-desthiobiotin, the protein was eluted by TEV cleavage on the column. The eluted sample was further purified by anion exchange chromatography on a 5 mL HiTrap Q column (GE Healthcare), which separated the free RAPTOR from mTORC1. Fractionations containing mTORC1 were concentrated to 1 mg/mL, frozen in liquid nitrogen and stored at -80 ºC. Strep-tagged RAPTOR alone was purified by StepTrap, HiTrap Q and gel filtration in a buffer consisting of 50 mM HEPES pH 7.5, 100 mM NaCl and 1 mM TCEP.

Three different RAPTOR variants bearing mutations in the region that contacts Rag GTPases were expressed. These mutants (RAPTOR_WC(593,594)AA, RD(597,598)AA and TDH(634-636)AAA) were purified by chromatography on a StrepTrap and HiTrap Q 5 mL columns, followed by gel filtration in a buffer consisting of 50 mM HEPES pH 7.5, 100 mM NaCl and 1 mM TCEP. The purified Strep-tagged-RAPTOR-WT and mutants were primarily used for the *in vitro* Strep-tag pull-down assays of tagless RagA/C.

### *In vitro* Strep-tag pull-down assays

Either purified Strep-tagged RAPTOR or Strep-tagged mTORC1 at a final concentration of 1 μM were incubated for 30 min on ice with StrepTactin Sepharose High Performance (GE Healthcare, 28-9355-99), which had been equilibrated with reaction buffer (50 mM HEPES pH 7.0, 150 mM NaCl, 1 mM TCEP, 2 mM $MgCl_2$, 5% glycerol). The protein-bound beads were washed with reaction buffer, after which the relevant binding partners were added to the beads. Samples of input/total reactions were taken, and after 60 min of incubation on ice, the beads were washed at least 3-6 times, and the samples were taken and analyzed by 4-12% SDS-PAGE, and visualized by InstantBlue staining (Expedeon, ISB1L). The binding partners had no Strep-tag, but were incubated with StrepTactin Sepharose beads and washed in the same way as the above reactions, in order to check whether they bind to empty beads. Rag heterodimers had no background binding to StrepTactin Sepharose resin. The gel intensity quantification of InstantBlue stained gels was performed using Image Lab (version 6, Bio-Rad Laboratories). Reactions were performed in three independent reactions.

### SEC-MALS

RagA/C/RAPTOR complex and free components including RAPTOR, Rag GTPases heterodimer and PRAS40 were analyzed by SEC-MALS at 4 °C using a Wyatt Heleos II 18-

angle light scattering instrument and Wyatt Optilab rEX online refractive index detector (Wyatt Technology Corporation).

The complex of RAPTOR with the Rag heterodimer (RagA-$Q66L_{GTP}$/RagC-$T90N_{GDP}$) in the ratio of 1:1.2 (at 15 mg/mL total protein concentration) was run at 4 °C on on a PROTEIN KW-803 column (Shodex TSK column, E904003) at 0.4 mL/min in 50 mM HEPES pH 7.0, 150 mM NaCl, 1 mM TCEP, 2 mM $MgCl_2$ buffer before passing through the light scattering and refractive index detectors in a standard SEC-MALS format.

The sample of full-length human PRAS40-WT (at 2 mg/mL) was run at room temperature on a Superdex 75 10/300 column (GE Healthcare) at 0.5 mL/min in 50 mM HEPES pH 7.5, 150 mM NaCl, 1 mM TCEP buffer in identical format (Fig. S4B).

Protein concentration was determined from the excess differential refractive index based on a 0.186 refractive index increment for a protein solution (1 g/mL) or the ultraviolet signal using 1.004 absorbance units/cm for 1 mg/mL. The concentration and the observed scattered intensity at each point in the chromatogram were used to calculate the absolute molecular mass from the intercept of the Debye plot using the Zimm model as implemented in Wyatt's ASTRA software. Autocorrelation analysis of data from the dynamic light scattering detector was also performed using Wyatt's ASTRA software and the translational diffusion coefficients determined were used to calculate the hydrodynamic radius using the Stokes-Einstein equation and the measured solvent viscosity of $9.3 \times 10^{-3}$ poise.

**Hydrogen-Deuterium exchange Mass Spectrometry (HDX-MS)**

HDX was performed, analysed and presented in a manner that meets the standards suggested by the HDX-MS community (*50*).

RAPTOR/Rag HDX-MS: Solutions consisting of 7.5 µM full-length human RagA-$Q66L_{GTP}$/RagC-$T90N_{GDP}$ or 7.5 µM Strep-FLAG-RAPTOR were incubated either in the

presence or absence of 11 μM RAPTOR or RagA/C, respectively, for 1 h on ice in a buffer consisting of 50 mM HEPES pH 7.5, 2 mM $MgCl_2$, 150 mM NaCl and 1 mM TCEP. An aliquot of 5 μL of protein was incubated at room temperature with 45 μL $D_2O$ Buffer (50 mM HEPES pH 7.5, 2 mM $MgCl_2$, 150 mM NaCl, 1 mM TCEP, 91.4% $D_2O$) for five timepoints (0.3, 3. 30, 300, 3000 s, the 0.3s was achieved by incubating proteins with ice-cold $D_2O$ buffer for 3s). Exchange reactions were quenched by addition of 20 μL of ice-cold Quench Buffer (2M Guanidinium chloride and 2.4% formic acid) then rapidly frozen in liquid nitrogen, prior to storage at -80 °C.

RAPTOR/PRAS40 HDX-MS: The samples were prepared as for RAPTOR/Rag HDX-MS.

Comparison of active and inactive Rag states: 5 μM solutions of either human RagA(Q66L)$_{GTP}$/RagC(A40-I399)-T90N$_{GDP}$ or RagA(T21N)$_{GDP}$/RagC(A40-I399)-Q120L$_{GTP}$ were prepared in a buffer consisting of 50 mM HEPES pH 7.5, 2 mM $MgCl_2$, 150 mM NaCl and 1 mM TCEP. An aliquot of 5 μL of protein was incubated at room temperature with 45 μL $D_2O$ Buffer (50 mM HEPES pH 7.5, 2 mM $MgCl_2$, 150 mM NaCl, 1 mM TCEP, 94.6% $D_2O$) for five timepoints (0.3, 3. 30, 300, 3000 s, the 0.3s was achieved by incubating proteins with ice-cold $D_2O$ buffer for 3s). Exchange reactions were quenched by addition of 20 μL of ice-cold Quench Buffer (2M Guanidinium chloride and 2.4% formic acid) then rapidly frozen in liquid nitrogen, prior to storage at -80 °C.

Data Acquisition and Analysis: For measurements, each sample was thawed and injected onto an M-Class Acquity UPLC with HDX technology (Waters) kept at 0.1 °C. The proteins were digested on an Enzymate Pepsin column (Waters, 186007233) at 15 °C for two minutes. Peptic peptides were then eluted onto an Acquity UPLC BEH C18 column (Waters, 186002346), equilibrated in Pepsin-A buffer (0.1 % formic acid), using a 3-43% gradient of Pepsin-B buffer (0.1% formic acid, 99.9% acetonitrile) over 22 minutes. Data were collected on a Waters Synapt G2-Si, with an electrospray ionization source, from 50 to 2000 m/z. All exchange

reactions were conducted in triplicate. The spray voltage was 3.0 kV. Data were collected in HDMS$^e$ mode. Peptides were identified from the non-deuterated samples of either RagA/C or RAPTOR, using the ProteinLynx Global Server (Waters). Three replicates were used to identify non-deuterated peptides. Criteria for including peptides for HDX analysis were as follows: a minimum intensity of 5000 counts, a maximum length of 25 residues, a minimum of three identified fragment ions, with an intensity of 0.1 products per amino-acid and a maximum mass error of 10 ppm. Data for peptides satisfying all of these criteria were input to the DynamX (Waters) software for automated data analysis. All peptide spectra were then manually inspected for sufficient quality (signal-to-noise, clear deuteration envelope and EX2 kinetics) for inclusion within the data set.

Colouring of the RagA/RagC ribbon diagram by HDX-MS: For each peptide, the average percent difference was calculated over all time points. The ribbon diagram was colored by this value for each peptide. The color for any given residue in the diagram was assigned based on the shortest peptide containing that residue.

**Crystallization of RagA/C heterodimers**

Purified RagA-Q66L$_{GTP}$/RagC(34-399)-T90N$_{GDP}$ was concentrated to approximately 20 mg/mL. The complex readily crystallised in the 2000 condition LMB screen (*51-53*). Initial crystal hits were optimized in both sitting and hanging drops by vapour diffusion plates at room temperature with a 1:1 (v/v) ratio of protein to reservoir solution. Thin clustered crystals were obtained in drops derived from condition H3 of the Morpheus II crystallization screen (*53*) which contains 100 mM MOPSO, Bis-Tris pH 6.5, 40 mM polyamines (spermine tetrahydrochloride, spermidine trihydrochloride, 1,4-diaminobutane dihydrochloride, 0.1 M D/L-ornithine monohydrochloride), 10% w/v PEG 8000 and 20% v/v 1,5-Pentanediol. Crystals were optimized by an iterative seeding approach, using micro- and macroseeding from thin

crystals. Final single crystals were grown for 27 days in drops containing 0.5 µL protein and 0.5 µL reservoir solution (same as H3 condition of the Morpheus II and with the final volume of PEG 8000 to 20% (w/v)), and were soaked in mother liquor containing 24% (v/v) glycerol prior to freezing in liquid $N_2$. Crystals for RagA-Q66L$_{GTP}$/RagC(40-399)-S75N$_{GDP}$ was crystallised and cryoprotected in the same way.

**Crystal structure determination and refinement**

Diffraction data for RagA/C crystals were collected at ID30A and ID30B beamline at ESRF (Grenoble) and DLS i04 beamline. Data were processed using XDS (*54*) and phases were determined by molecular replacement using GTPase domain from RagC (PDB ID 3LLU) and the RagA/C C-terminal roadblock domain (CRD) (*35*) as search models in PHASER (*55*). The protein was built using Coot (*56*), refined using Refmac5 (*57*), and validated with a MolProbity (*58*) (Table S2). All crystallography related structure figures were generated in PyMol Molecular Graphics System, Version 1.8.2.2 (Schrödinger).

**Cryo-EM sample preparation**

Prior to mixing the mTORC1 complex with the PRAS40-fused-RagA/C or RagA/C for the formation of mTORC1-PRAS40-fused-RagA/C or mTORC1-RagA/C complexes, the purified individual mTORC1 complex and PRAS40-fused-RagA/C or RagA/C underwent buffer exchange using Ultra-0.5 mL Ultra-100K concentrator (Millipore, UFC510096) and Ultra-50K concentrator (Millipore, UFC505096), respectively, into buffer consisting of 50 mM HEPES pH 7.0, 100 mM NaCl, 1 mM TCEP and 5 mM $MgCl_2$. For the mTORC1-PRAS40-fused-RagA/C complexes, a solution of 1 µM mTORC1 was mixed with a solution of 60 µM RagA-Q66L$_{GTP}$/PRAS40-fused-RagC-T90N$_{GDP}$ complex and incubated for 60 min at 4 °C. The solution was then concentrated to approximately 0.4 mg/mL. The complex was stabilized and

further purified by GraFix ultracentrifugation (*59*). An aliquot of 320 µL of the protein complex was pre-incubated on ice for 1 hour, and then 0.03% glutaraldehyde was added and further incubated for 35 min prior to loading onto an 8 mL 10% to 30% glycerol gradient containing 0.0 to 0.2% glutaraldehyde (Sigma, G5882). Gradient was formed from 50 mM HEPES, pH 7.0 (RT), 100 mM NaCl, 2 mM $MgCl_2$, 1 mM TCEP and either 10% [v/v] glycerol with no glutaraldehyde or 30% glycerol with 0.2% glutaraldehyde. Gradients were centrifuged at 235125 g in a Beckman SW40 rotor (Beckman Coulter, Krefeld, Germany) for 14 h at 4 °C. Successive fractions of 250 µL were collected from the top of the tube and analyzed by SDS-PAGE. The cross-linked material was pooled and quenched with 100 mM Tris-HCl pH 8.0. The protein was concentrated in an Ultra-15 Ultracel 100K concentrator (Millipore, UFC910024), purified by SEC on a Superose 6i 10/300 column (GE Healthcare) and concentrated to a final concentration of 0.06 $OD_{280}$ and immediately used in cryo-EM grid preparation. Prior to freezing grids, Tween20 (Thermo Scientific, 28320) was added from a 0.05% stock to the sample to give a final concentration of 0.005% to obtain a proper ice thickness.

mTORC1-RagA-$Q66L_{GTP}$/RagC(40-399)-$T90N_{GDP}$ samples for cryo-EM were prepared similarly to the above approach used for the mTORC1-PRAS40-fused-RagA/C sample, except that mTORC1 was incubated with 1 mM AMPPNP (Jena Bioscience, NU-407-10) prior to incubating with RagA/C complex, and a different crosslinking procedure was used. First, samples were incubated with 0.24 mM BS3 (Thermo Scientific, 21585) for 30 min on ice, and then they were incubated with 0.1% of glutaraldehyde for 30 min and quenched with 100 mM Tris-HCl pH 7.0. After crosslinking, a two-step purification was carried out, including glycerol gradient ultracentrifugation using a gradient as described for the mTORC1-PRAS40-fused RagA/C, except without glutaraldehyde, and finally, the crosslinked fractions were

subjected to gel filtration and the samples were concentrated to a final concentration of 0.6 $OD_{280}$.

**Cryo-EM data collection and processing**

For the mTORC1-RagA-$Q66L_{GTP}$/PRAS40-fused-RagC-$T90N_{GDP}$ complex, a layer of graphene oxide (GO, Sigma, 777676) was used to cover Holey carbon Quantifoil Au R 2/2 (200 mesh) grids. GO-covered grids were prepared as described previously (*60*). Prior to covering the grids with GO, they were glow-discharged using an Edwards Sputter Coater S150B for 60 s at 40 mA. An aliquot of 3 µL of the purified mTORC1-PRAS40-fused RagA/C complex was added to GO-covered grids (added on the carbon side and incubated for 15 s), blotted for 10 s at 10 °C and then plunge-frozen in liquid ethane using an FEI Vitrobot Mark IV (Thermo Fisher). We collected a total of 7130 micrographs of the human mTORC1-PRAS40-fused RagA/C complex on an FEI Titan Krios electron microscope operated at 300 keV. Zero-energy loss images were recorded on a Gatan K2 Summit direct electron detector operated in super-resolution mode with a Gatan GIF Quantum energy filter (20 eV slit width) using EPU automated data collection (ThermoFisher) for automated data collection. Images were recorded at a calibrated magnification of 34,965 (pixel size of ~1.43 Å) with an exposure rate of ~1.8 electrons/$Å^2$/s. An overall exposure of 11 s was fractionated into 22 movie frames adding to a total exposure of approximately 40 electrons/$Å^2$. For data collection, a defocus range of -3.2 to -1.8 µm was used.

While the mTORC1-RagA-$Q66L_{GTP}$/PRAS40-fused-RagC-$T90N_{GDP}$ sample was applied onto GO-supported grids, the sample of mTORC1 complex with non-tagged RagA-$Q66L_{GTP}$/RagC(40-399)-$T90N_{GDP}$ was applied to glow-discharged Quantifoil Au R 1.2/1.3 (300 mesh) grids with no additional support. Grids were blotted for 3 s at 18 ºC, with approximately 99% humidity and plunge-frozen in liquid ethane using an FEI Vitrobot Mark

IV. For this mTORC1-RagA/C sample, a total of 3453 micrographs were acquired on a FEI Titan Krios electron microscope operated at 300 keV. The entire dataset was collected using a similar approach to the above described mTORC1-PRAS40-fused RagA/C dataset.

**Image processing**

All image-processing steps were done using RELION3 (*61*), which includes Gctf (*62*), MotionCor2 (*63*) and ResMap (*64*). A total of 7130 micrographs of mTORC1-PRAS40-fused RagA/C were processed using GPU-accelerated MotionCor2 to correct for electron beam-induced sample motion, while contrast transfer function (CTF) parameters were determined using Gctf. Reference-based autopicking was performed using RELION3 with initial templates obtained from a previous mTORC1-PRAS40-fused RagA/C dataset.

In total 1,208,875 particles were extracted with a particle box size of 400 by 400 pixels. Two rounds of reference-free 2D classification (using a mask with a diameter of 350 Å) resulted in a selection of 580,707 particles. This set of particles was subjected to a 3D classification over 35 iterations in point group $C_1$ using a low-pass filtered (60 Å) ab-initio reference, which was created using the SGD algorithm for de-novo 3D model generation introduced in RELION3. This resulted in six reasonable classes. To correct for beam-induced particle movements and to apply radiation-damage weighting, the refined particles were further 'polished' using the Bayesian approach implemented in RELION3. Following this step, another 3D autorefinement in C2 using a mask around the mTORC1-RagA/C complex as well as applying solvent-flattened FSCs yielded a reconstruction of 4.4 Å resolution based on the gold-standard FSC = 0.143 criterion (*65*, *66*) (Fig. S5).

After per-particle CTF, defoci and beamtilt values were refined for the complete set of selected particles, a subsequently performed 3D autorefinement resulted in a mTORC1-RagA/C reconstruction of 4.3 Å resolution (FSC = 0.143 criterion). After correction for the

detector modulation transfer function (MTF) and B-factor sharpening, the post-processed map was used for inspection in CHIMERA (*67*) and model building in Coot (*68*). Local resolutions were estimated using ResMap.

Given that we could not be sure that every mTORC1 particle has two Rag heterodimers bound to it, we used a strategy taking advantage of the relion_particle_symmetry_expand program (*32*). We duplicated the C2-refined particles (resulting in a total of 1,161,414 particles) and applied the appropriate rotation and translation to generate a set of monomers. The previous structure of mTORC1 used an approach with 'pseudo-monomer' to improve the overall resolution (*3*). mTOR has four domains (Fig. 2A): the N-HEAT (or spiral), the M-HEAT (or bridge), the FAT and the kinase domain (*3*, *69-71*). The cryo-EM structure of mTORC1 showed that flexibility within the two mTOR molecules in the mTORC1 dimer causes the N-HEAT to track the motion of the dimer-related M-HEAT more closely than it does the FAT domain to which it is covalently, but flexibly attached (*3*). The pseudo-monomer was formed by simply swapping the two N-HEAT domains from the mTOR dimer (*3*). Using focused classification with signal subtraction on the expanded C1 set of pseudo-monomer particles yielded four reasonable classes with a total of 947138 good particles. In this focused classification, we kept the orientations fixed at the values determined in the original refinement without performing any new particle alignment. This approach led to a reconstruction of 4.1 Å resolution, based on the gold-standard FSC = 0.143 criterion (Fig. S6A). We observed density associated with the α-solenoid region of RAPTOR that we assumed was due to the PRAS40-fused RagA/C, however, it was quite broken with no distinct secondary structural features, hence we performed focused classification with signal subtraction on this region of extra density. We obtained one reasonable class and the number of particles associated with this class was 90,809. Following 3D auto-refinement of these mTORC1-PRAS40-fused RagA/C

particles, we obtained a reconstruction of 5.5 Å resolution that readily fitted the crystal structure of RagA/C heterodimer that we determined by X-ray crystallography.

The processing of mTORC1-RagA/C dataset was similar to the strategy used for the mTORC1-PRAS40-fused RagA/C. A combined dataset of 3453 micrographs yielded to a total of 169,971 good particles, this set of particles were then polished and CTF refined as described above. The 3D auto-refinement in C2 using a mask around the mTORC1-RagA/C complex as well as applying solvent-flattened FSCs yielded a 6.4 Å resolution reconstruction. Applying the symmetry-expanded pseudo-monomer strategy resulted in 241,306 particles. Focused classification with signal subtraction yielded four well-defined classes, with 136,987 particles. These were subjected to a 3D refinement, yielding a 4.9 Å resolution reconstruction. This EM density map clearly showed the presence of extra EM density for the RagA/C. Focused classification with signal subtraction to the extra density region provided reasonably looking classes that were pooled to give 51902 particles. The subsequent 3D auto-refinement of these mTORC1-RagA/C particles led to a 6.2 Å resolution reconstruction into which the Rag heterodimer from our X-ray crystal structure could be readily fit (Fig. S8A). The highest local resolution was in the kinase domain of mTOR (Fig. S8C).

A particle orientation efficiency score (*72*), Efficiency ($E_{od}$) of 0.58 and 0.7 for grids prepared with and without graphene-oxide support, respectively (Figs. S5D,S7C), suggested that the graphene-oxide datasets has a minor Fourier space gap in the 3D electron densities volumes and probably slightly hampered the final resolution. No 3D deformation related to poor particle distribution was observed in processed datasets. The directional resolutions of the final cryo-EM maps were analyzed for both mTORC1/RagA/C data sets. A lower standard deviation from the mean of the directional FSC and higher sphericity for the mTORC1/non-tagged RagA/C indicate more uniform sampling of particle orientations (*73*) (Figs. S5E,S7D).

**Cryo-EM structure refinement**

Cryo-EM model of mTORC1-Rag GTPase heterodimer was refined using REFMAC5 program in CCPEM package, with a composite map of the 3D reconstruction of mTORC1-RagA/C pseudomonomer of one protomer together with the generated map for the other 'second' protomer of mTORC1-RagA/C. This second protomer of mTORC1-RagA/C map was generated by simply aligning the first 3D reconstructed pseudomonomer map onto the mTORC1 dimer consensus C2 map and then obtained the rotation-translation matrix with CHIMERA (*67*) and then used Maputils program in CCP4i. From the resulting mTORC1-RagA/C dimer map, the model of mTORC1-RagA/C was built by using previously published structure of apo-mTORC1 (*3*) and here-obtained crystal structure of Rag GTPases heterodimer was fitted into the extra density of RAPTOR α-solenoid region. The entire mTORC1-RagA/C final model was refined using REFMAC5 program using the restraints from the crystal structure of RagA/C and previously published mTORC1 structure (PDB ID 6BCX). Side chains were removed before refinement, since these were not evident in the cryo-EM densities. Separate model refinements were performed against single half-maps, and the resulting models were compared with the other half-maps to confirm the absence of overfitting (Fig. S6E, S8B).

## Supplementary Figures

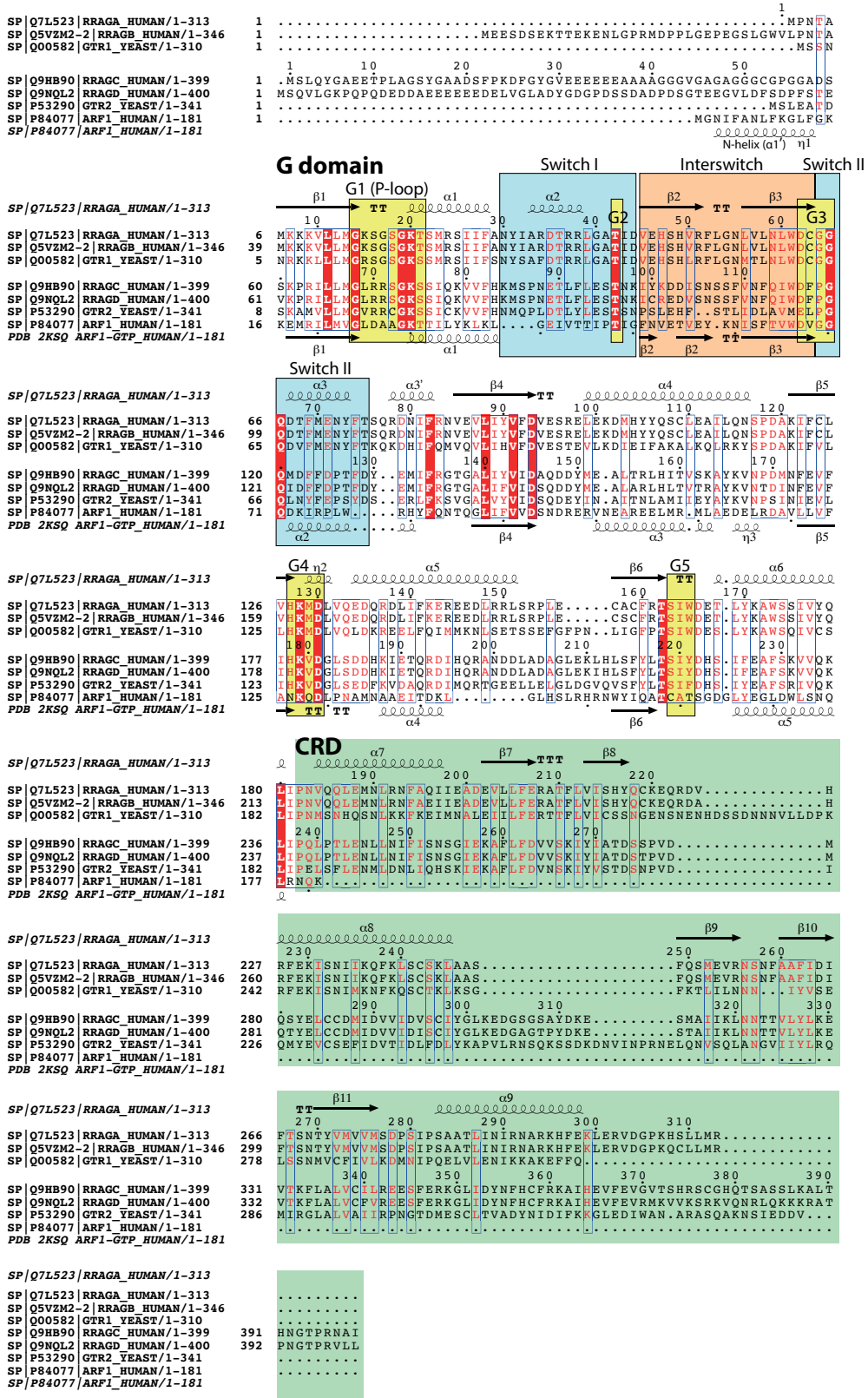


**Figure S1. Sequence alignment of Rag GTPases.**

A sequence alignment of RagA homologues (RagB and Gtr1) with RagC orthologues (RagD and Gtr2). The secondary structure elements of RagA from our crystal structures are illustrated

above the sequence. The sequence of human Arf1 is shown below the RagC orthologues, with secondary structure elements from the $Arf1_{GTP}$ complex (PDB ID 2KSQ(*74*)) below it. The conserved nucleotide-binding elements (G-motifs, switch I, interswitch and switch II) are highlighted.

5

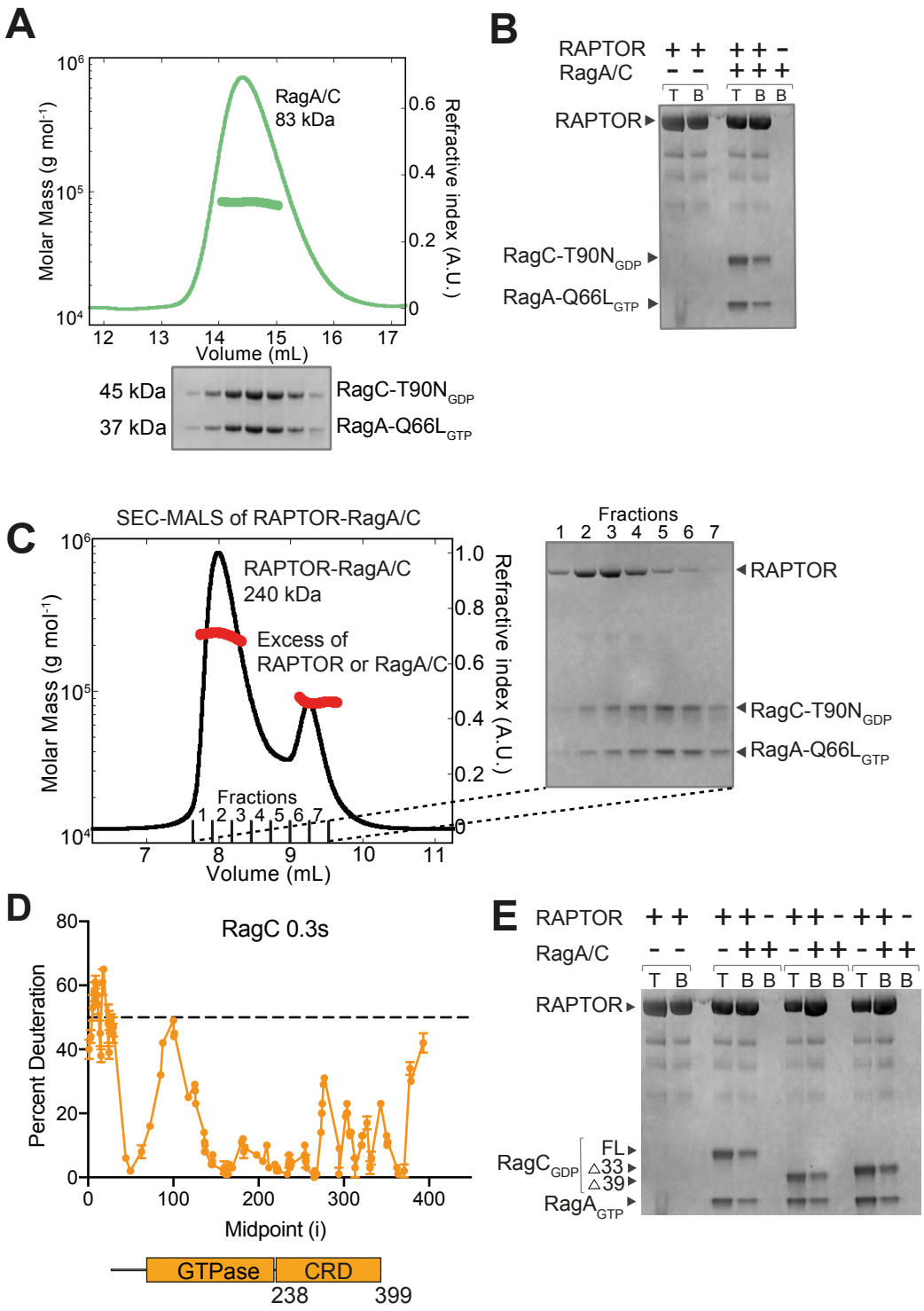


**Figure S2. Characterization of a recombinant RagA/C and its interaction with RAPTOR.**

(**A**) SEC-MALS shows RagA-Q66L$_{GTP}$/RagC-T90N$_{GDP}$ is monodisperse with the expected mass.

(**B**) *In vitro* pull-down showing Strep-tagged RAPTOR binding to RagA-Q66L$_{GTP}$/RagC-T90N$_{GDP}$. The lanes for the total input (T) and for the Strep-Tactin bound fraction (B) are indicated. Full gel in Fig. S13.

(**C**) SEC-MALS chromatogram for a RAPTOR-RagA/C mixture. The fitted molecular masses (red) are consistent with the expected 238 kDa RAPTOR-RagA/C complex and excess of individual components. Right: Coomassie-stained SDS-PAGE for fractions.

(**D**) A graphical plot for deuterium uptake of RagC at the 0.3 s timepoint. The dotted line marks 50% deuteration. Peptides with a deuterium uptake >50% after 0.3 s exposure to deuterium are likely to be highly disordered. The N-terminus of RagC was identified as very likely intrinsically disordered.

(**E**) Deleting this flexible N-terminal region of RagC does not affect binding to either RagA or the RagA/C complex to RAPTOR, as shown by the *in vitro* pull-down assays of Strep-tagged RAPTOR and RagA/C heterodimers with N-terminal truncations of RagC and SDS-PAGE analysis. The lanes for the total input (T) and for the bound fractions (B) are indicated.

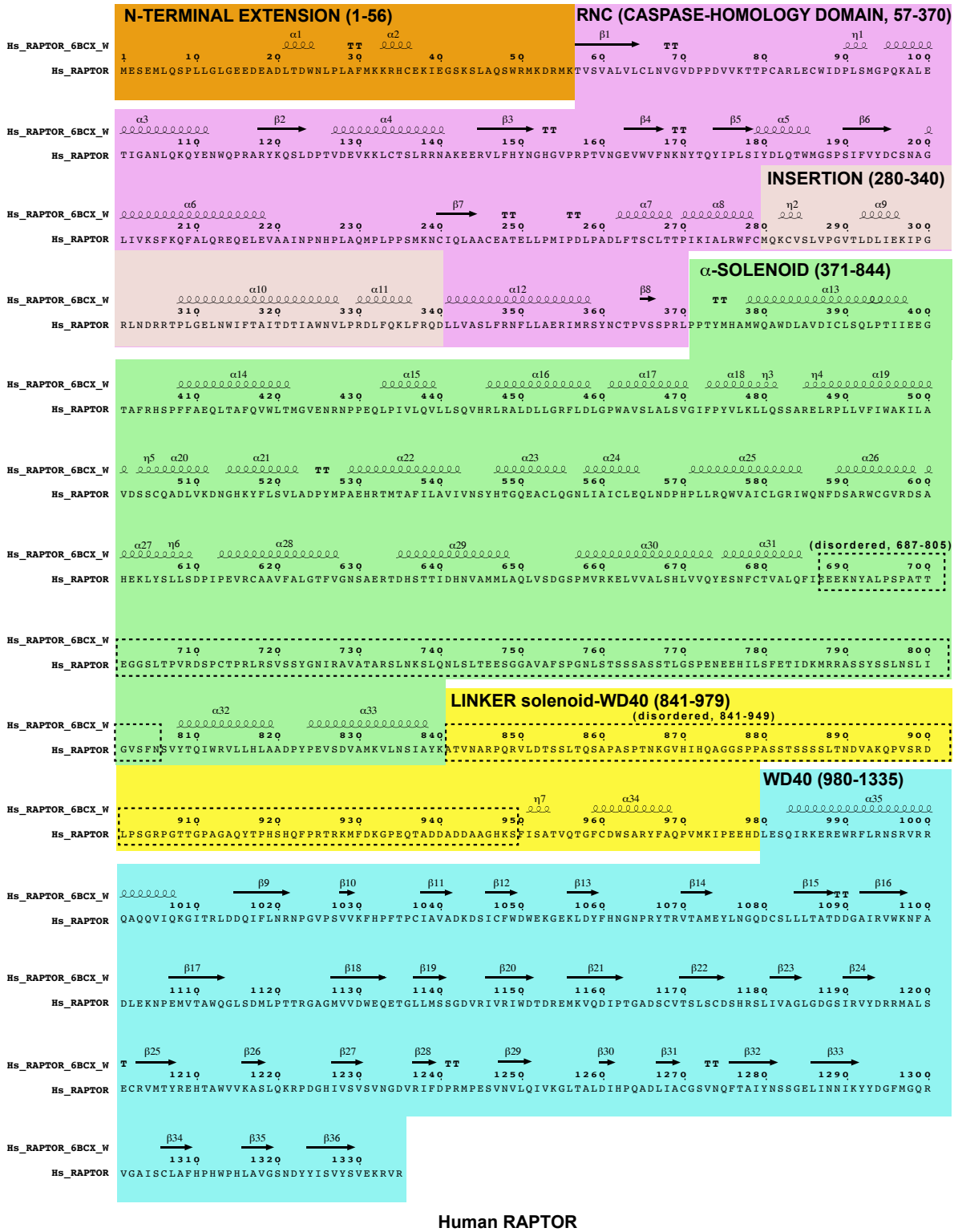


**Figure S3. Secondary structure and domain organization of human RAPTOR.**

Colored blocks denote RAPTOR domains. The secondary structure elements are numbered and shown above the sequence.

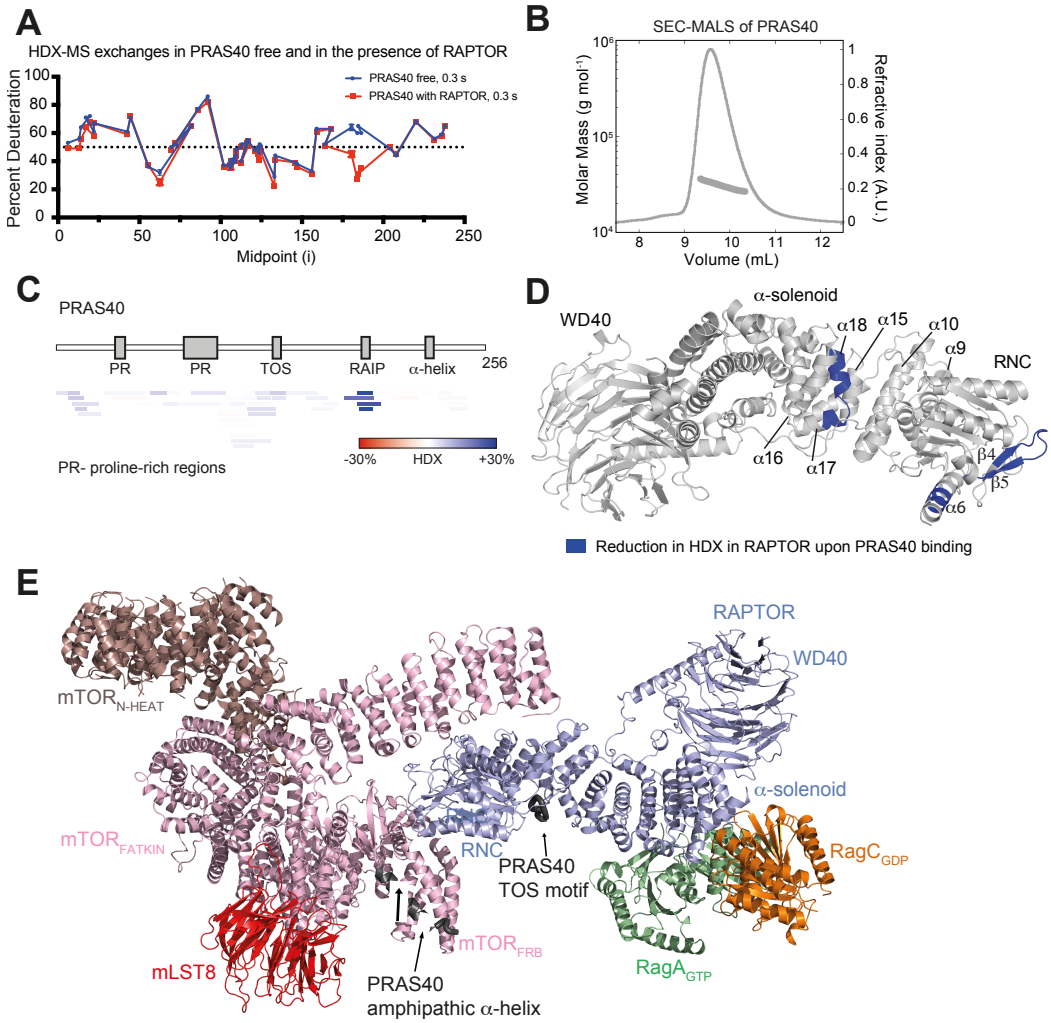


**Figure S4. Structural details of mTORC1 interaction with PRAS40.**

(**A**) HDX-MS plot for PRAS40 in the apo state (blue) or bound to RAPTOR (red), for 0.3 s timepoint in D2O. Each point represents the mean percent deuteration, shown as the midpoint of a single peptic peptide (with triplicate measurements shown with error bars). The dotted line marks 50% deuteration. Previous studies have shown that regions that exhibit >50% deuteration at 0.3 s deuterium exposure are likely to be intrinsically disordered. Detailed results are shown in Table S3.

(**B**) SEC-MALS profile and the fitted molecular mass for PRAS40 (gray).

(**C**) Schematic diagram of PRAS40 displayed together with differences in HDX at the 0.3 s timepoint for all the peptides of PRAS40 upon binding to RAPTOR. Each coloured bar beneath

the PRAS40 schematic represents a peptide, where the colour of that peptide denotes the change in solvent exchange rate that occurs on addition of RAPTOR.

(**D**) Decreases in HDX (blue) in RAPTOR upon PRAS40 binding are depicted on the three-dimensional structure of RAPTOR (PDB code: 6BCX, RAPTOR). Two regions of RAPTOR, namely the region at the N-terminus of RNC domain, and the groove between RNC and α-solenoid are protected from solvent exchange upon PRAS40 binding.

(**E**) Cryo-EM structure of mTORC1-PRAS40-fused-RagA/C, with only half of the dimeric complex shown. Two regions from PRAS40 (colored black), namely, TOS motif and PRAS40 amphipathic α-helix are visible in the structure. The mTORC1 components are colored as in Fig. 2A-C.

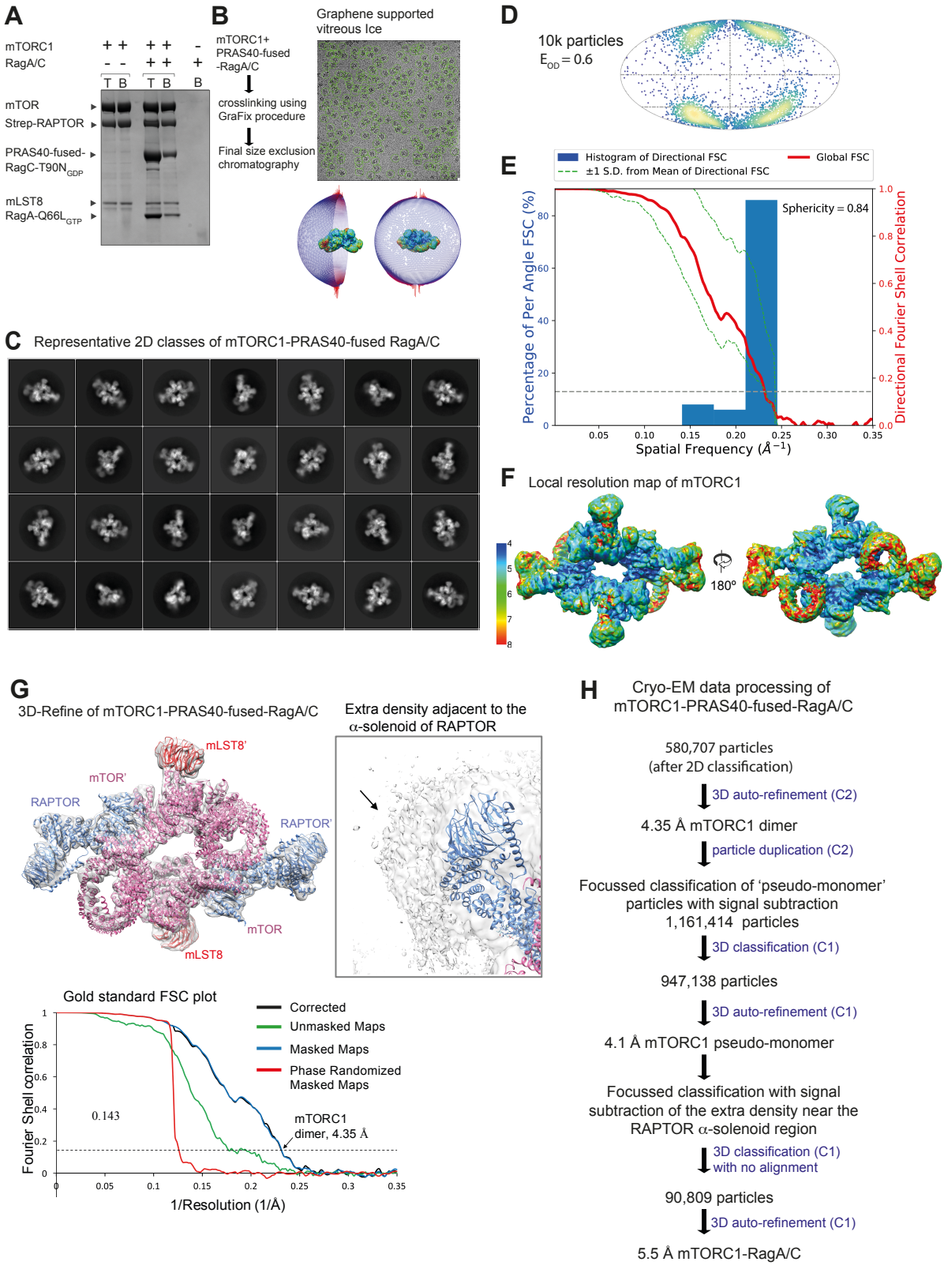


**Figure S5. Experimental strategy for the cryo-EM reconstruction of mTORC1 complex with PRAS40-fused-RagA/C**

(**A**) SDS-PAGE gel shows the Strep-pull-down assay, confirming the binding of mTORC1 to the PRAS40-fused-RagA/C GTPases (abbreviated as 'tagged-RagA/C'). The mTORC1 complex bound to StrepTactin resin via Strep-tagged RAPTOR was incubated with tagged RagA/C complexes and the pulled-down proteins were analysed by Coomassie-stained SDS-PAGE. The lanes for the total input (T) and the bound fraction (B) are shown.

(**B**) Representative micrographs of cryo-EM grids prepared with graphene oxide support. mTORC1-containing particles are circled (green). The angular distribution (Euler angles) of the last 3D auto-refinement indicates some over-represented views (preferred orientation, red cylinders).

(**C**) Some of the representative 2D classes are shown for the mTORC1/tagged-RagA/C.

(**D**) The orientation distributions are plotted on a Mollweide projection for mTORC1/tagged-RagA/C. Each point represents an observed particle and the color scale represents the calculated normalized probability density of observing a particle in a particular orientation. $E_{od}$ is the efficiency of each orientation distribution (*72*). Efficiencies suggested that the graphene-oxide datasets have a minor Fourier space gap in the 3D electron densities volumes and probably slightly hampered the final resolution. No obvious anisotropy was observed in the cryo-EM maps.

(**E**) Directional resolution of the final cryo-EM maps of mTORC1/tagged-RagA/C.

(**F**) The local resolutions of the 3D-reconstructions are shown for the mTORC1/tagged-RagA/C together with the resolution bar ranging from 4 Å to 8 Å (blue to red gradient).

(**G**) Gold-standard FSC plot for the reconstruction of masked mTORC1/tagged-RagA/C dimer and the cryo-EM density (transparent surface view) displayed together with the refined atomic model. Inset shows the extra density for RagA/C adjacent to the α-solenoid of RAPTOR with the highest relative level of density.

(**H**) Flowchart of cryo-EM data processing for the mTORC1/tagged-RagA/C.

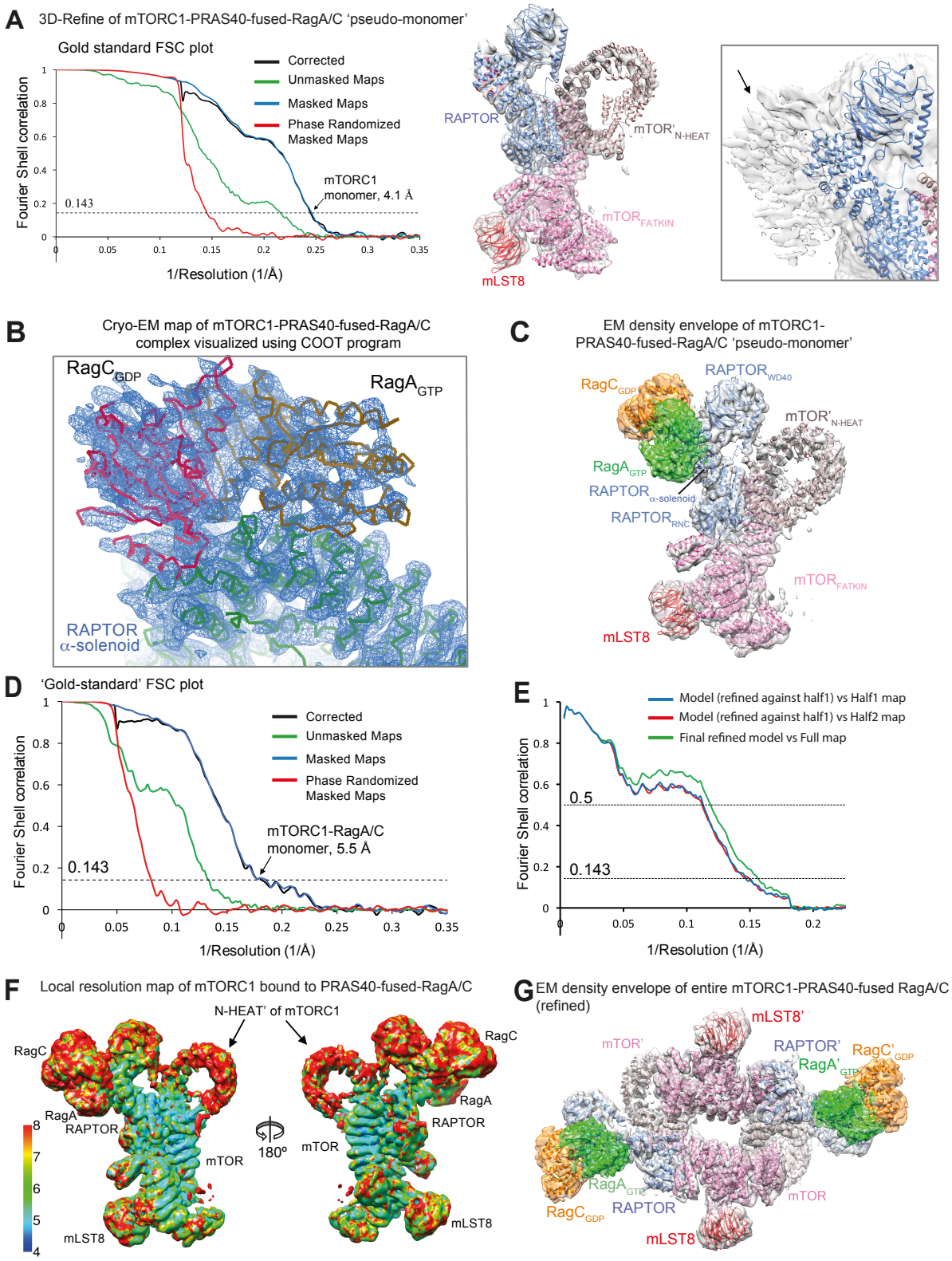


**Figure S6. Cryo-EM reconstruction of mTORC1 complex with PRAS40-fused-RagA/C.**

(**A**) Gold-standard FSC plot for the reconstruction of mTORC1/tagged-RagA/C 'pseudo-monomer' after particle duplication (C2) and focused classification with signal subtraction in

the mTORC1 'pseudo-monomer' (see Methods) and the cryo-EM density envelope of mTORC1/tagged-RagA/C (transparent surface view) displayed together with the refined atomic model. Inset shows the extra density for RagA/C adjacent to the α-solenoid of RAPTOR.

(**B**) Focused classification with density subtraction in the RagA/C region revealed cryo-EM density for Rag heterodimers, resulting in a 5.5 Å resolution reconstruction (**D**) into which our high-resolution RagA-RagC structure could be fit. Density shown for the region using COOT.

(**C**) Cryo-EM density of the mTORC1/tagged-RagA/C 'pseudo-monomer' dataset.

(**D**) Gold-standard FSC plot for the reconstruction of masked monomer with signal subtraction of mTORC1/tagged-RagA/C, the FSC cutoff and the estimated resolution are shown.

(**E**) Fourier shell correlation curves of the final model versus the full map (green), of a model refined in the first independent half map versus the first half map (blue), and of the same model versus the second independent half map, which was not used for refinement (red). The line indicates the FSC value for 0.143 and 0.5.

(**F**) The local resolution of the 3D-reconstruction is shown for the focused classified particles containing mTORC1/tagged-RagA/C with the resolution bar ranging from 4 Å to 8 Å (blue to red gradient).

(**G**) Cryo-EM density envelope of the entire mTORC1/tagged-RagA/C dimer (transparent surface view) together with the generated atomic model is visualized as similar to Fig. 2B.

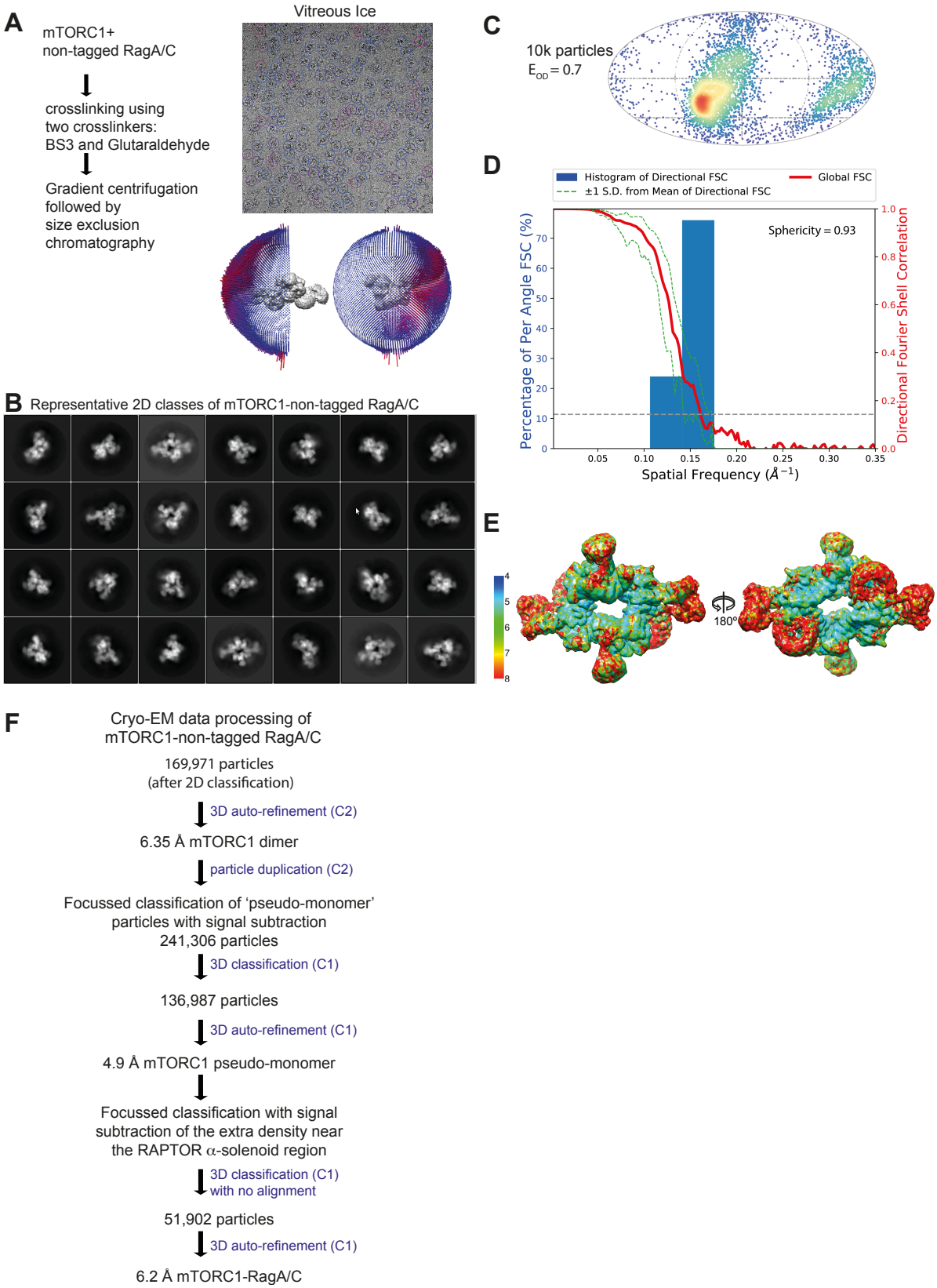


**Figure S7. Experimental strategy for the cryo-EM reconstruction of mTORC1 in complex with non-tagged RagA/C.**

(**A**) Representative micrographs of cryo-EM grids prepared in vitreous ice for mTORC1/non-tagged-RagA/C (RagA/C is not fused to PRAS40). The angular distribution of the last 3D auto-refinement indicates more uniform particle distributions.

(**B**) Some of the representative 2D classes are shown for the mTORC1/non-tagged-RagA/C.

(**C**) The orientation distributions are plotted on a Mollweide projection for mTORC1/non-tagged-RagA/C and the $E_{od}$ is annotated.

(**D**) Directional resolution of the final cryo-EM maps of mTORC1/non-tagged-RagA/C. A lower standard deviation from the mean of the directional FSC and higher sphericity indicate more uniform sampling of particle orientations(*73*).

(**E**) The local resolutions of the 3D-reconstructions are shown.

(**F**) Flowchart of cryo-EM data processing for mTORC1/non-tagged-RagA/C.

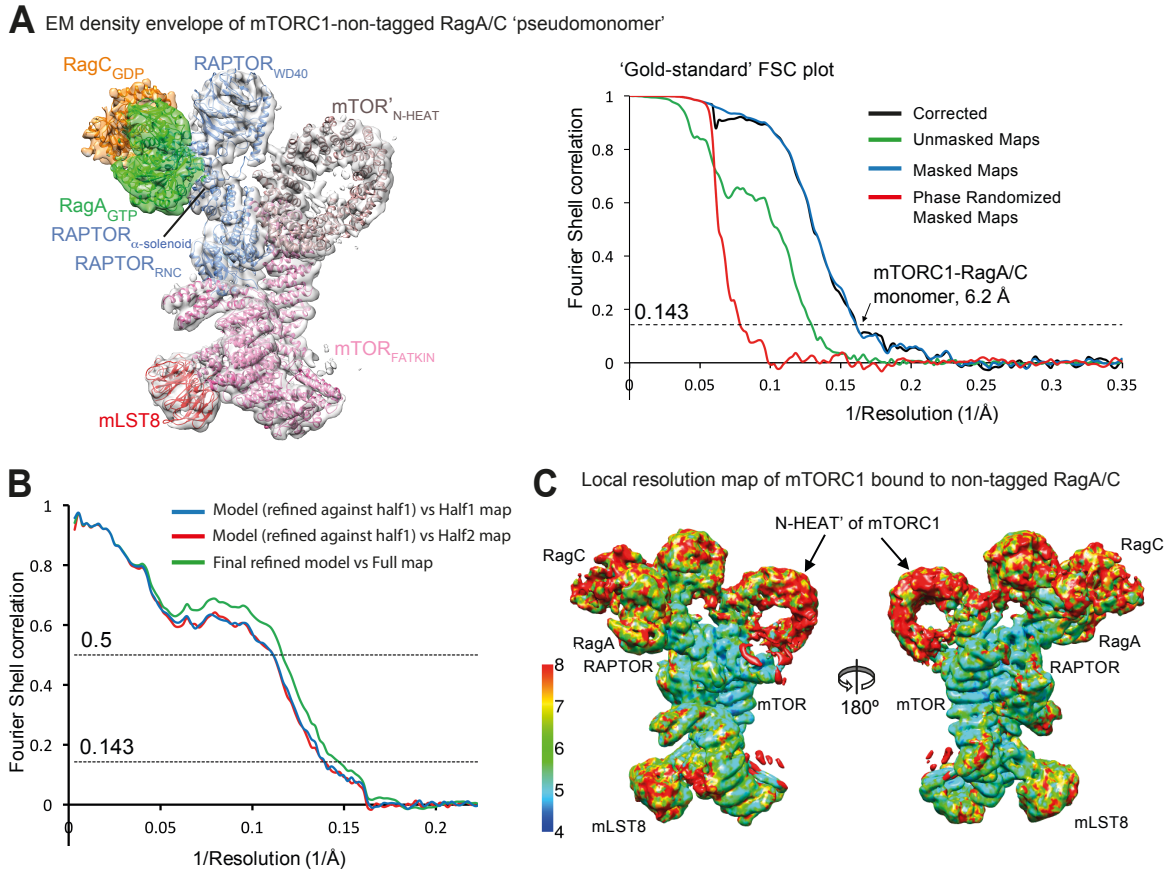


**Figure S8. Cryo-EM reconstruction of mTORC1 in a complex with non-tagged RagA/C.**

(**A**) Cryo-EM density envelope of the mTORC1/non-tagged-RagA/C 'pseudo-monomer' dataset. Gold-standard FSC plot for the reconstruction of masked monomer of this mTORC1/non-tagged-RagA/C 'pseudo-monomer', the FSC cut-off and the estimated resolution are annotated.

(**B**) Fourier shell correlation curves of the final model versus the full map (green), of a model refined in the first independent half map versus the first half map (blue), and of the same model versus the second independent half map, which was not used for refinement (red). The line indicates the FSC value for 0.143 and 0.5.

(**C**) The local resolution of the 3D-reconstruction is shown for the focused classified particles containing only mTORC1/non-tagged-RagA/C.

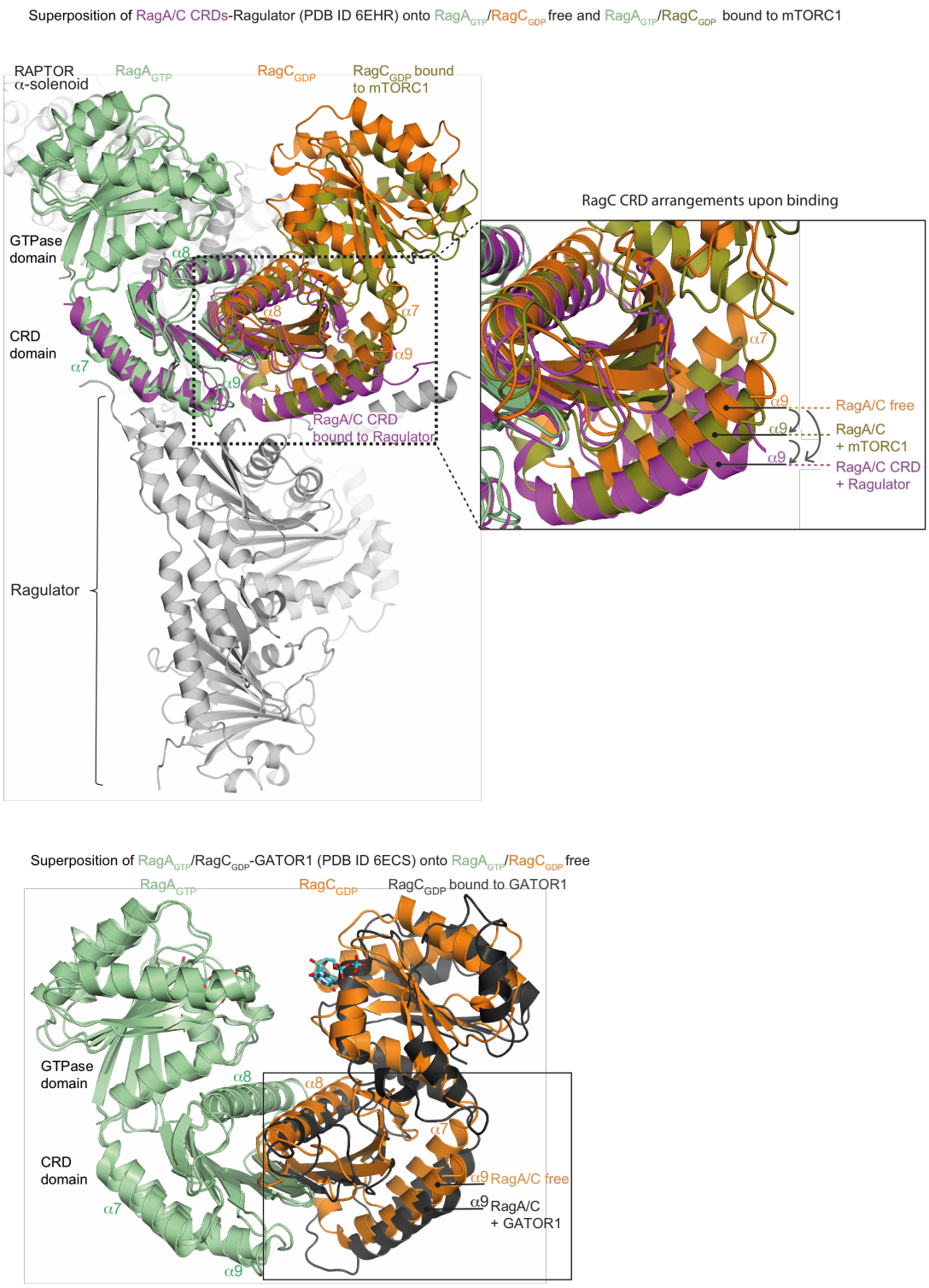


**Figure S9. Structural comparisons of free RagA/C and RagA/C bound to mTORC1 or Ragulator.**

Comparison of free RagA/C (from the crystal structure of RagA-Q66L$_{GTP}$/RagC-T90N$_{GDP}$) with RagA/C bound to mTORC1 and with the RagA/C CRD domains bound to the Ragulator

(PDB ID 6EHR). The CRD α9 helices of RagC in the three structures are indicated to highlight the shift in the relative orientation of the CRD domains. Superposition was on the RagA subunit. A similar shift between the two CRDs in a heterodimer is seen in the cryo-EM structure of RagA/C bound to GATOR1 (PDB ID 6CES (*75*)) relative to our free RagA/C structure (lower panel).

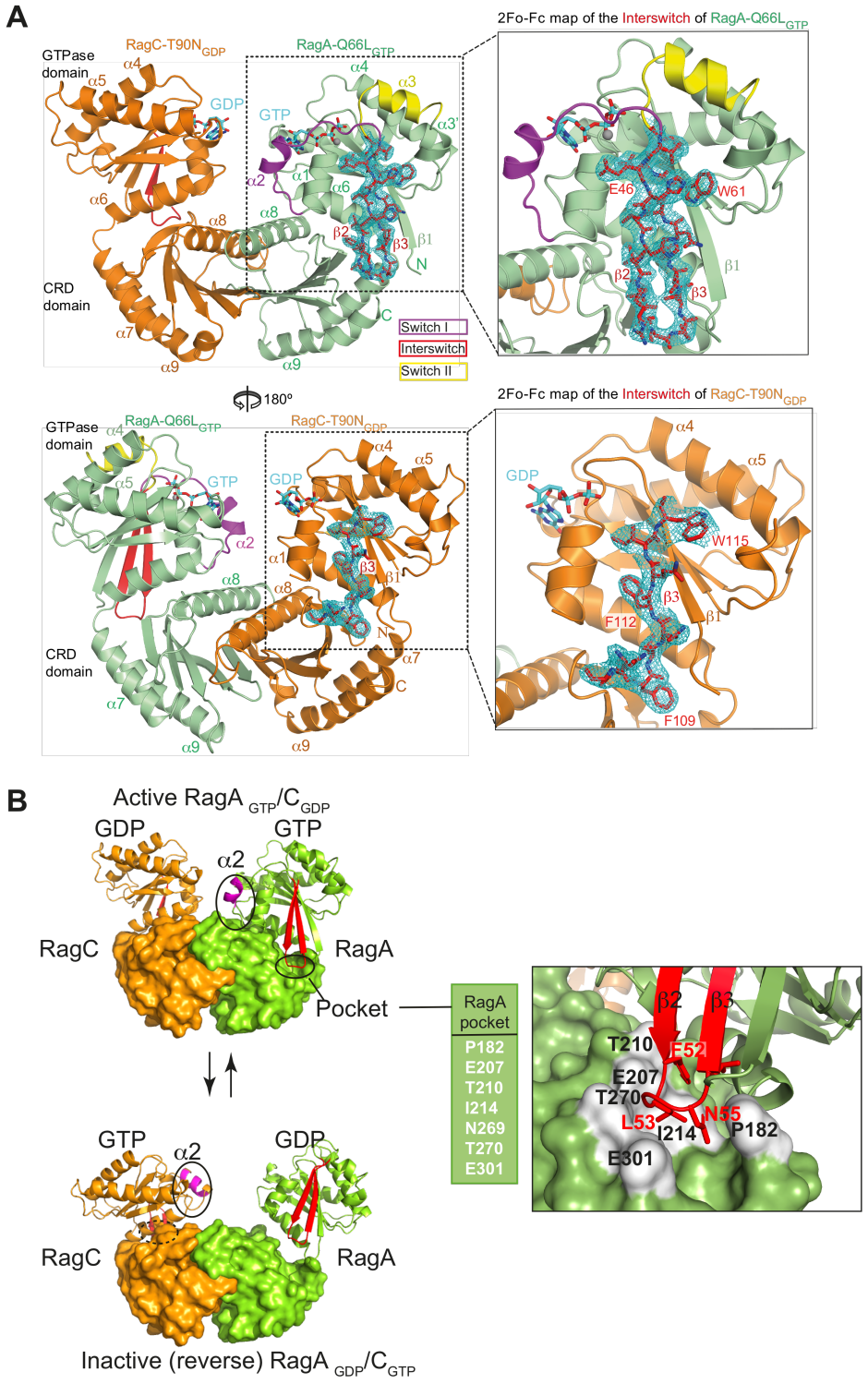


**Figure S10. The crystal structure of a RagA/C heterodimer and a model for interdomain communication in the Rag heterodimers.**

(**A**) A PyMOL representation of the 2mFo-DFc electron density map (contoured at 1.2σ) covering the interswitch regions of crystal structure of RagA-Q66L$_{GTP}$/RagC(34-399)-T90N$_{GDP}$.

(**B**) A cartoon illustrating the structural basis for nucleotide-dependent communication between the two GTPase domains and between the GTPase domains and the CRDs in the Rag heterodimers. Two elements of the communication are highlighted, helix α2 of switch I (magenta) and the β2/β3 interswitch (red). When GTP binds to one GTPase domain, it triggers ordering of switch I, interswitch and switch II. The interswitch undergoes a register shift that extends it into a pocket on the surface of the CRD into which it locks (the pocket is shown for $RagA_{GTP}$). The GTP-dependent conformational changes alter the orientations of the GTPase domains, so that GTP binding in one domain inhibits binding and simulates GTP hydrolysis by the paired domain. The $RagC_{GDP}$ has switches mostly disordered and the interswitch hairpin retracted, but upon GTP binding it undergoes switch ordering along with a register shift and interswitch extension similar to RagA.

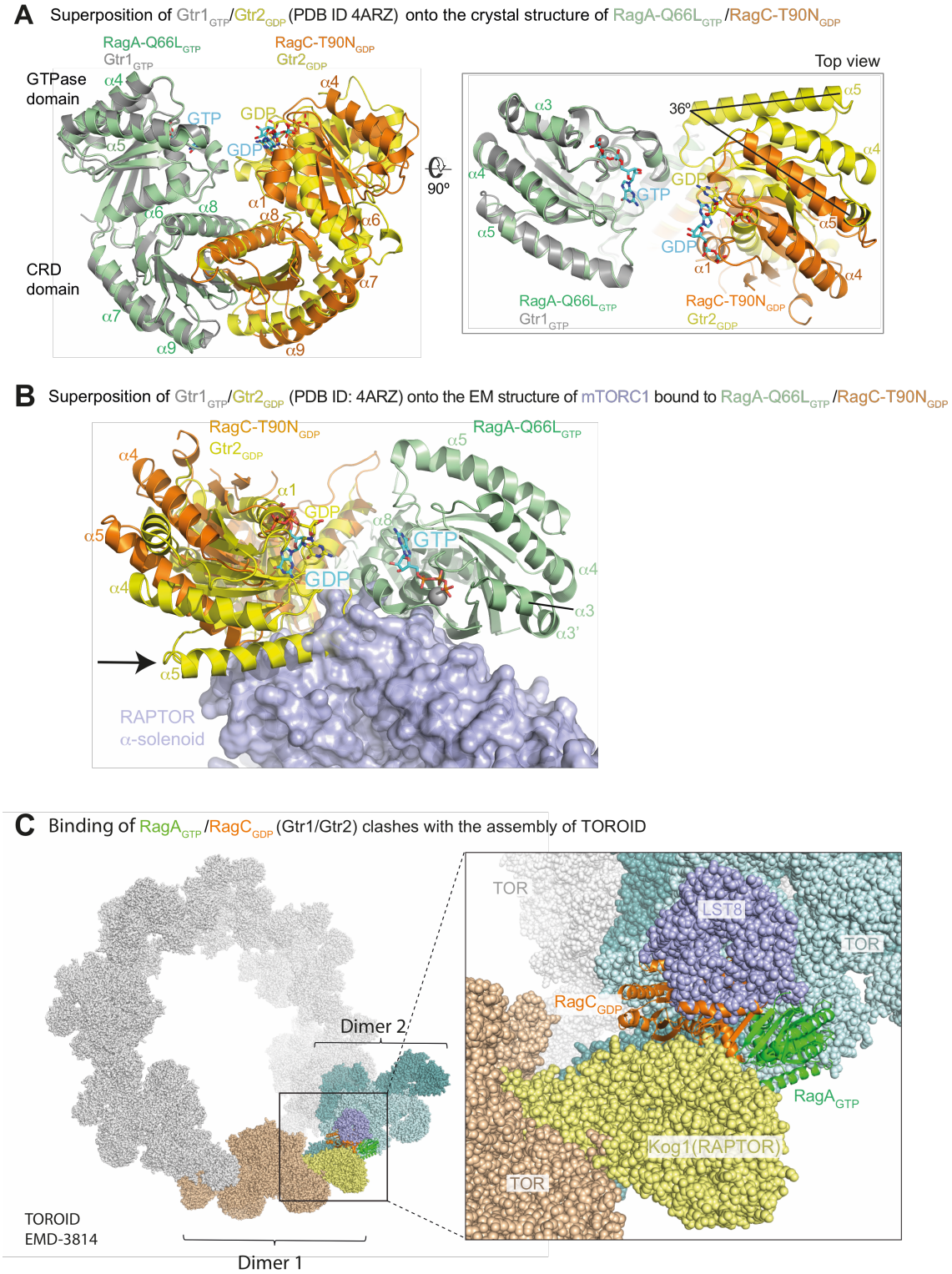


**Figure S11. Structural insight into regulation of TORC1 in yeast from the RagA/C/mTORC1 organization.**

(**A**) Comparison of RagA-Q66L$_{GTP}$/RagC-T90N$_{GDP}$ with Gtr1$_{GTP}$/Gtr2$_{GDP}$ (PDBID 4ARZ). RagA was superimposed on Gtr1. The inset illustrates the change in the Gtr2$_{GDP}$ orientation with respect to RagC$_{GDP}$.

(**B**) Comparison of RagA-$Q66L_{GTP}$/RagC-$T90N_{GDP}$ bound to mTORC1 with $Gtr1_{GTP}$/$Gtr2_{GDP}$ (PDBID 4ARZ). RagA was superimposed on Gtr1. The RAPTOR subunit to which RagA/C is bound is shown as a surface, illustrating that there would have to be a change in the orientation of Gtr2 with respect to the conformation in the yeast crystal structure in order to bind to the yeast orthologue of RAPTOR.

(**C**) An illustration of the architecture of a TOROID tube, an inactive organization of TORC1 formed in response to glucose starvation (*40*). Human mTORC1 was fit into the cryo-EM density (EMD-3814) to build the model. The inset illustrates a contact in the TOROID between the Kog1 (RAPTOR) subunit in one TORC1 dimer with a TOR subunit in a neighboring TORC1 dimer in the helical tube. Gtr1/2 ($RagA_{GTP}$/$RagC_{GDP}$, green/orange ribbon) binding to its interface on Kog1 would clash with Tor and Lst8, possibly preventing assembly of the TOROID.

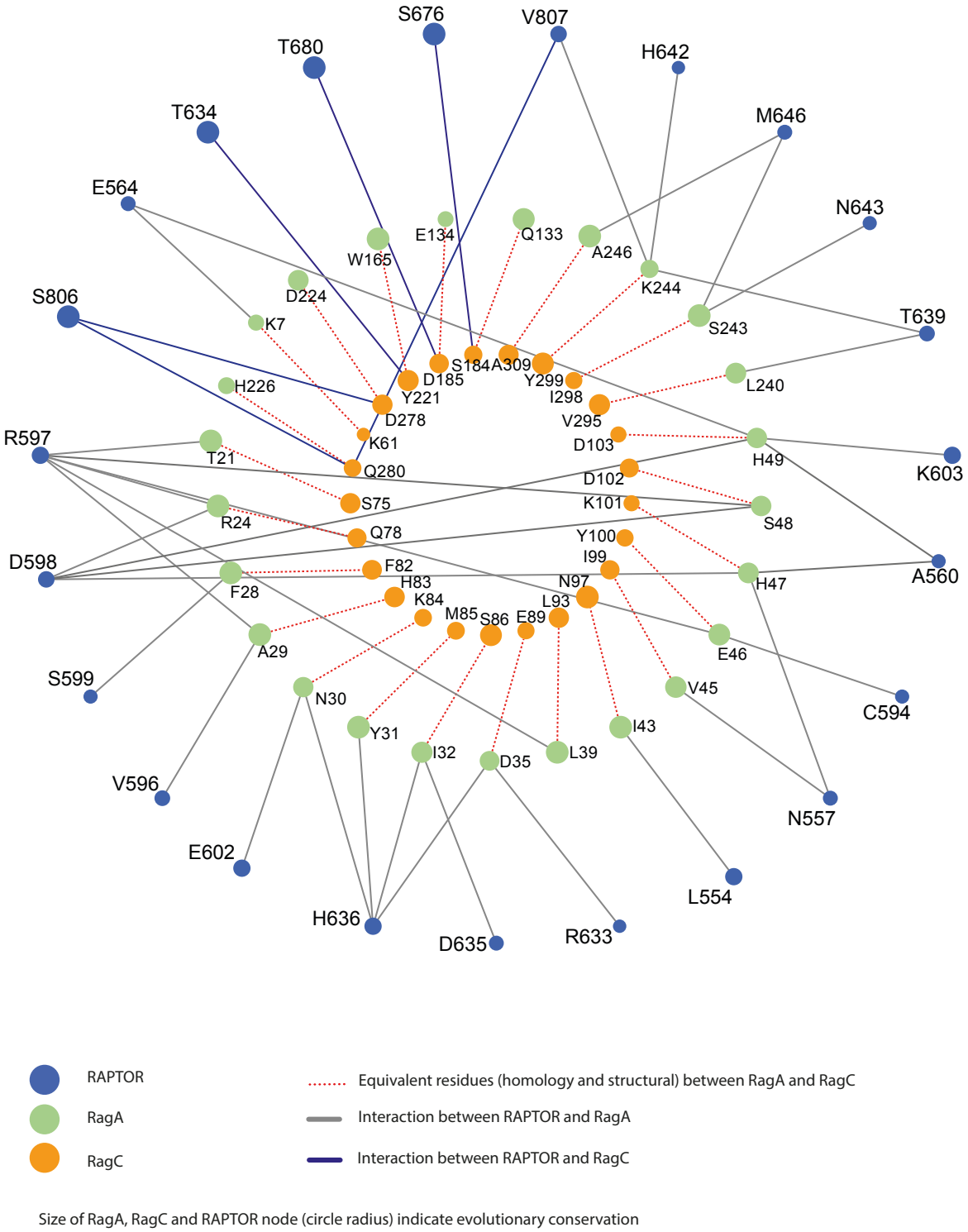


**Figure S12. Conservation of residues involved in the interaction between RagA/C and RAPTOR.**

RAPTOR residues (outer, blue ring) interacting with RagA (middle, green ring) are indicated by grey lines and those interacting with RagC (inner, orange ring) by blue lines. RagA residues are connected by dotted red lines to the equivalent residues in RagC. The

diameters of the circles indicate the degree of conservation of a given residue in the separate sequence alignments of orthologs for the three proteins: RAPTOR, RagA and RagC. Larger circles indicate greater conservation. RagA residues, which form most of the interface with RAPTOR are more conserved. For the alignment, selected sequences for RAPTOR, RagA and RagC from Protozoa, Fungi and Animalia were used (Homo sapiens, Branchiostoma floridae, Drosophila melanogaster, Nematostella vectensis, Trichoplax adhaerens, Capsaspora owczarzaki, Saccharomyces cerevisiae, Dictyostelium discoideum, Paramecium tetraurelia, Thalassiosira pseudonana, Emiliania huxleyi, Leishmania major and Naegleria gruberi).

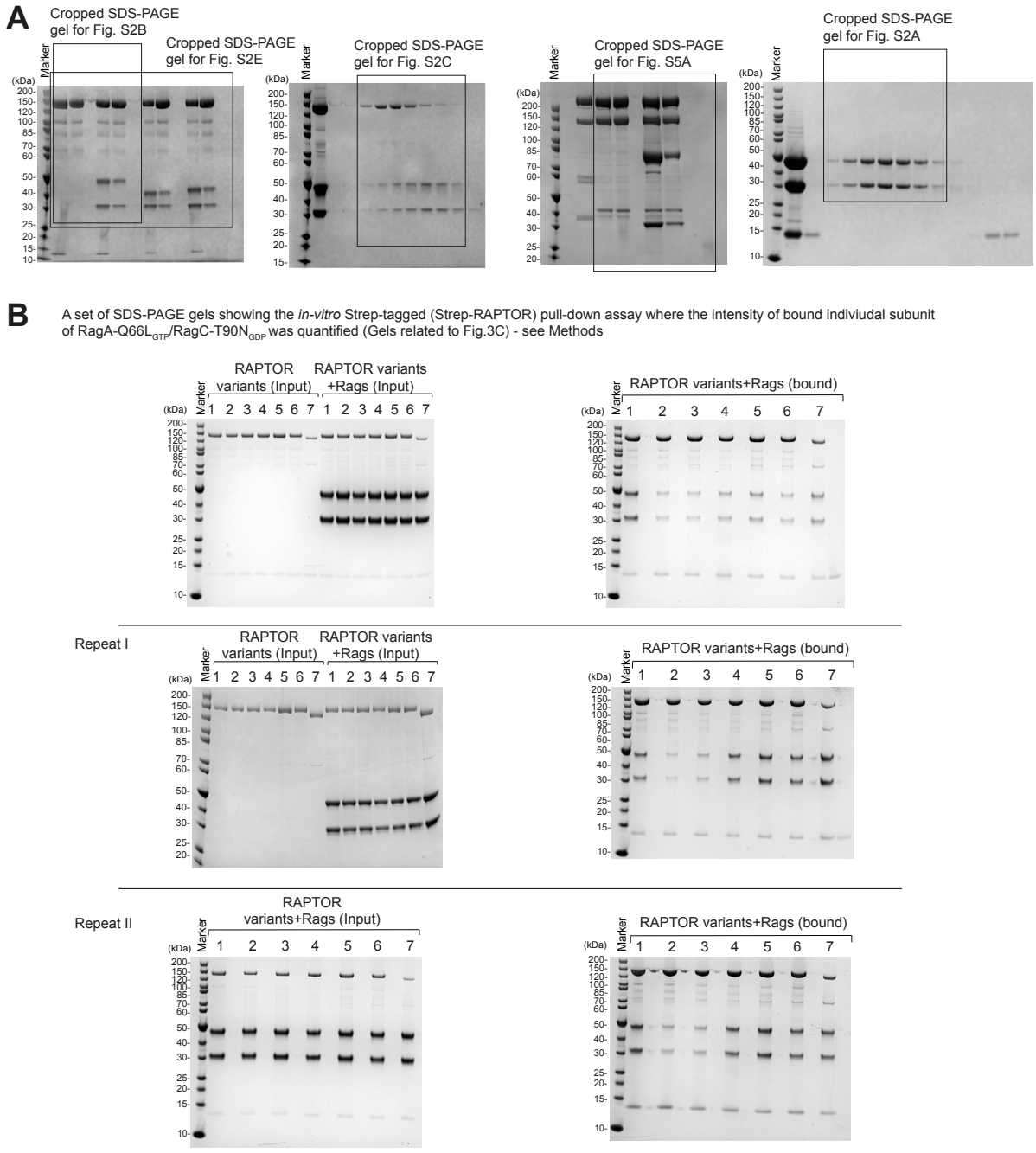


**Figure S13. A complete image of SDS-PAGE gels used in this study.**

(**A**) The cropped parts of the SDS-PAGE gels are shown for the respective figures as indicated. (**B**) SDS-PAGE gels showing the *in vitro* pull-down assay related to Fig. 3C are shown. Three independent reactions were carried out. Each set of reactions comprised of two gels relating to their input and bound of total reactions as indicated.

**Movie S1. Conformational changes in RagA/C upon binding to mTORC1.**

A PyMOL morph of the structure of free RagA-$Q66L_{GTP}$/RagC-$T90N_{GDP}$ (from crystal structure) into RagA/C bound to mTORC1 (cryo-EM). The movie begins with the RagA/C in the free conformation. In the middle, the RagA/C is in the mTORC1-bound conformation. Before morphing, the RagA/C free and mTORC1 bound were aligned on the RagA subunit (pale green). The movie shows the change in the orientation of RagC (orange). The RAPTOR subunit of mTORC1 from the bound structure is visible (light blue).

**Movie S2. A model for the conformational changes between the active and reverse (inactive) states of RagA/C.**

A PyMOL morph between the active state, $RagA_{GTP}/C_{GDP}$ (crystal structure of RagA-$Q66L_{GTP}$/RagC-$T90N_{GDP}$), and a model for the reverse (inactive) state, $RagA_{GDP}/RagC_{GTP}$. The reverse state was modeled based on $RagC_{GTP}$ (PDB ID 3LLU) and $RagA_{GDP}$ was modeled based on $RagC_{GDP}$. The model is colored according to differences in HDX for the two states (as in Fig. 5D). The switches were modeled in both states to illustrate all of the HDX-MS differences. The switches disappear in the GDP-bound states, to illustrate their disorder.

**Table S1. HDX-MS analysis of the interaction between human RagA-Q66L$_{GTP}$/RagC-T90N$_{GDP}$ and human RAPTOR.**

The table presents the HDX for each peptic peptide of each protein at each time point (0.005, 0.05, 0.5, 5 and 50 min) for RagA/C alone (7.5 μM) or with RAPTOR (11 μM) and for RAPTOR alone (7.5 μM) or with RagA/C (11 μM). The summary presents differences in HDX between free and bound states.

**Table S2. Crystallography data collection, phasing and refinement statistics**

| | RagA-Q66L$_{GTP}$/ RagC(34-399)-T90N$_{GDP}$ | RagA-Q66L$_{GTP}$/ RagC(40-399)-S75N$_{GDP}$ |
|---|---|---|
| **Data collection** | | |
| Space group | P $2_1$ $2_1$ $2_1$ | P $2_1$ $2_1$ $2_1$ |
| Cell dimensions | | |
| *a*, *b*, *c* (Å) | 72.10, 81.86, 244.08 | 71.5, 81.44, 246.03 |
| α, β, γ (°) | 90, 90, 90 | 90, 90, 90 |
| Wavelength | 0.9677 | 0.9762 |
| Resolution (Å) | 41.93 – 2.63 (2.74 – 2.63) | 49.24 – 2.50 (2.59-2.5) |
| *Rmeas* | 0.07 (1.588) | 0.077 (1.25) |
| $I / \sigma I$ | 17.9 (1.1) | 15.9 (1.7) |
| Completeness (%) | 0.98 (0.98) | 0.997 (0.98) |
| Rpim | 0.027 (0.59) | 0.029 (0.49) |
| $CC^{1/2}$ | 0.999 (0.492) | 0.999 (0.588) |
| CC* | 1 (0.81) | 1 (0.86) |
| **Refinement** | | |
| Resolution (Å) | 49.63 – 2.64 | 49.24 – 2.50 |
| No. reflections all/free | 43094 (4256) / 2102 (227) | 50584 (4926) / 2457 (243) |
| Rwork / Rfree (%) | 19.9/26.1 | 20.9/27.6 |
| No. atoms | | |
| Protein | 9325 | 9396 |
| Ligand/ion | 143 (GTP, GDP, $Mg^{2+}$) | 136 (GTP, GDP, $Mg^{2+}$) |
| Water | 73 | 52 |
| *Average B*-factors | 97.5 | 78.6 |
| Protein | 97.8 | 79 |
| Ligand/ion | 92.4 | 66 |
| Water | 82.3 | 67 |
| R.m.s deviations | | |
| Bond lengths (Å) | 0.017 | 0.015 |
| Bond angles (°) | 2.19 | 2.07 |
| Ramachandran plot (%) Favoured, allowed, outliers | 87.6, 9.8, 2.6 | 89.4, 8.3, 2.3 |
| MolProbity | 2.8 | 2.7 |
| PDB code | 6S6A | 6S6D |
| Beamline | DLS I04 and ESRF ID30A3, ID30B | |

[a]One crystal was used for data collection and refinement.

[b]Values in parentheses are for highest-resolution shell.

**Table S3. HDX-MS analysis of the interaction between human PRAS40 and human RAPTOR.**

The table presents the HDX for each peptic peptide of each protein at each time point (0.005, 0.05, 0.5, 5 and 50 min) for PRAS40 alone (7.5 μM) or with RAPTOR (11 μM) and for RAPTOR alone (7.5 μM) or with PRAS40 (11 μM). The summary presents differences in HDX between free and bound states.

**Table S4. Cryo-EM data collection and processing of mTORC1 in complex with RagA/C**

| | mTORC1-PRAS40-fused-RagA/C | mTORC1-non-tagged RagA/C |
|---|---|---|
| **Cryo-EM data collection and processing** | | |
| Protein details | mTORC1 in complex with RagA-Q66L$_{GTP}$/PRAS40-fused-RagC-T90N$_{GDP}$ | mTORC1 in complex with RagA-Q66L$_{GTP}$/ RagC(40-399)-T90N$_{GDP}$ |
| Microscope | Titan Krios | Titan Krios |
| cryo-EM grids | Graphene-oxide covered Quantifoil R2/2 Au200 | Quantifoil R 1.2/1.3 Au300 (no support) |
| Magnification | 34,965 | 34,965 |
| Voltage (keV) | 300 | 300 |
| Detector and Mode | Gatan K2 Summit and counting mode | |
| Automation data collection software | EPU | |
| Defocus range (μm) | -1.8 to -3.2 | -1.8 to -3.2 |
| Electron exposure ($e^-$ / Å$^2$) | 39-40 | ~41 |
| Exposure rate ($e^-$ / Å$^2$/ s) | 1.7 - 1.8 | 1.8 - 1.9 |
| Number of frames collected | 22 | 22 |
| Energy filter slit width (eV) | 20 | 20 |
| Pixel size (Å) | 1.43 | 1.43 |
| No of Micrographs used | 7130 | 3453 |
| Total No. of extracted particles (after removing junk) | 580,707 | 169,971 |
| Particle orientation efficiency ($E_{od}$) score | 0.58 | 0.7 |
| Sphericity value | 0.84 | 0.93 |
| Global resolution of mTORC1 dimer ['Gold-standard' FSC 0.143 (Å)] | 4.4 | 6.4 |
| Total No. of refined particles after particle symmetry expand (C2 symmetry) | 1,161,414 | 241,306 |
| Focused classification of mTORC1-RagA/C 'pseudo-monomer' masked region with signal subtraction: | | |
| Global resolution of mTORC1 'pseudo-monomer', FSC 0.143 (Å) | 4.1 | 4.9 |
| Focused classification of RagA/C masked region with signal subtraction and 3D reconstruction of mTORC1-RagA/C 'pseudo-monomer': | | |
| No. of particles in final map of mTORC1 bound to RagA/C | 90,809 | 51,902 |
| Resolution of masked/unmasked maps of mTORC1-RagA/C ['Gold-standard' at FSC 0.143 (Å)] | 5.5 / 7.1 | 6.2 / 7.7 |
| Map sharpening *B* factor (Å$^2$) | 181 | 211 |
| **Refinement** | | |
| Initial model used | 6BCX, and 6S6A (this study) | |
| Refinement package | REFMAC5 and COOT real-space refinement | |

| | | |
|---|---|---|
| Model Resolution (Å) | 5.5 | 5.9 |
| No. atoms | | |
| Protein | 8306 | 8246 |
| Ligand/ion | 4 | 4 |
| $FSC_{average}$* | 0.8 | 0.83 |
| R factor | 0.3 | 0.34 |
| CC, overall | 0.9 | 0.78 |
| *B*-factors (Å$^2$) | | |
| Protein | 283.5 | 314.9 |
| Ligand/ion | - | - |
| R.m.s deviations | | |
| Bond lengths (Å) | 0.009 | 0.008 |
| Bond angles (°) | 1.8 | 1.7 |
| **Validation** | | |
| MolProbity score | 1.24 | 1.26 |
| Ramachandra plot | | |
| Favoured (%) | 92.2 | 92.5 |
| Allowed (%) | 7 | 6.6 |
| Disallowed (%) | 0.8 | 0.9 |
| CαBLAM (%outliers) | 2.7 | 2.7 |
| Cα geometry(%outliers) | 0.51 | 0.55 |
| PDB code | 6SB0 | 6SB2 |
| EMD code | EMD-10132 | EMD-10133 |

∗FSCaverage is calculated over the resolution bins up to 5.5 and 6.2 Å for mTORC1-PRAS40-fused-RagA/C and mTORC1-RagA/C, respectively.

**Table S5. Analysis of differences between active human RagA/C (RagA-Q66L$_{GTP}$/RagC-T90N$_{GDP}$) and inactive human RagA/C (RagA-T21N$_{GDP}$/RagC-Q120L$_{GTP}$).**

The table presents the HDX for each peptic peptide of RagA (**A**) or RagC (**B**) at each time point (0.005, 0.05, 0.5, 5 and 50 min) for active RagA/C (5 μM) or inactive RagA/C (5 μM). The summary presents differences in HDX between the two states.

**Supplementary References**

47. H. Teo, O. Perisic, B. Gonzalez, R. Williams, ESCRT-II, an endosome-associated complex required for protein sorting: crystal structure and interactions with ESCRT-III and membranes. *Dev. Cell*. **7**, 559–569 (2004).

48. N. G. Wallis, M. D. Allen, R. W. Broadhurst, I. A. Lessard, R. N. Perham, Recognition of a surface loop of the lipoyl domain underlies substrate channelling in the pyruvate dehydrogenase multienzyme complex. *J Mol Biol*. **263**, 463–474 (1996).

49. J. E. Burke *et al.*, Structures of PI4KIIIβ complexes show simultaneous recruitment of Rab11 and its effectors. *Science*. **344**, 1035–1038 (2014).

50. G. R. Masson *et al.*, Recommendations for performing, interpreting and reporting hydrogen deuterium exchange mass spectrometry (HDX-MS) experiments. *Nat Meth*. **16**, 595–602 (2019).

51. D. Stock, O. Perisic, J. Löwe, Robotic nanolitre protein crystallisation at the MRC Laboratory of Molecular Biology. *Prog. Biophys. Mol. Biol.* **88**, 311–327 (2005).

52. F. Gorrec, J. Löwe, Automated Protocols for Macromolecular Crystallization at the MRC Laboratory of Molecular Biology. *J Vis Exp*, e55790–e55790 (2018).

53. F. Gorrec, The MORPHEUS II protein crystallization screen. *Acta Crystallogr F Struct Biol Commun*. **71**, 831–837 (2015).

54. W. Kabsch, XDS. *Acta Crystallogr. D Biol. Crystallogr.* **66**, 125–132 (2010).

55. A. McCoy, Solving structures of protein complexes by molecular replacement with Phaser. *Acta Crystallogr. D Biol. Crystallogr.* **63**, 32–41 (2007).

56. P. Emsley, B. Lohkamp, W. G. Scott, K. Cowtan, Features and development of Coot. *Acta Crystallogr. D Biol. Crystallogr.* **66**, 486–501 (2010).

57. G. Murshudov *et al.*, REFMAC5 for the refinement of macromolecular crystal structures. *Acta Crystallogr. D Biol. Crystallogr.* **67**, 355–367 (2011).

58. V. B. Chen *et al.*, MolProbity: all-atom structure validation for macromolecular crystallography. *Acta Crystallogr. D Biol. Crystallogr.* **66**, 12–21 (2010).

59. H. Stark, GraFix: stabilization of fragile macromolecular complexes for single particle cryo-EM. *Meth. Enzymol.* **481**, 109–126 (2010).

60. A. Boland *et al.*, Cryo-EM structure of a metazoan separase-securin complex at near-atomic resolution. *Nat. Struct. Biol.* **24**, 414–418 (2017).

61. S. H. W. Scheres, RELION: implementation of a Bayesian approach to cryo-EM structure determination. *J. Struct. Biol.* **180**, 519–530 (2012).

62. K. Zhang, Gctf: Real-time CTF determination and correction. *J. Struct. Biol.* **193**, 1–12 (2016).

63. S. Q. Zheng *et al.*, MotionCor2: anisotropic correction of beam-induced motion for improved cryo-electron microscopy. *Nat Meth*. **14**, 331–332 (2017).

64. A. Kucukelbir, F. J. Sigworth, H. D. Tagare, Quantifying the local resolution of cryo-EM density maps. *Nat Meth*. **11**, 63–65 (2014).

65. S. H. W. Scheres, S. Chen, Prevention of overfitting in cryo-EM structure determination. *Nat Meth*. **9**, 853–854 (2012).

66. P. B. Rosenthal, R. Henderson, Optimal determination of particle orientation, absolute hand, and contrast loss in single-particle electron cryomicroscopy. *J Mol Biol*. **333**, 721–745 (2003).

67. E. F. Pettersen *et al.*, UCSF Chimera--a visualization system for exploratory research and analysis. *J Comput Chem*. **25**, 1605–1612 (2004).

68. P. Emsley, K. Cowtan, Coot: model-building tools for molecular graphics. *Acta Crystallogr. D Biol. Crystallogr.* **60**, 2126–2132 (2004).

69. H. Yang *et al.*, 4.4 Å Resolution Cryo-EM structure of human mTOR Complex 1. *Protein Cell*. **7**, 878–887 (2016).

70. C. H. S. Aylett *et al.*, Architecture of human mTOR complex 1. *Science*. **351**, 48–52 (2015).

71. D. Baretić, A. Berndt, Y. Ohashi, C. M. Johnson, R. L. Williams, Tor forms a dimer through an N-terminal helical solenoid with a complex topology. *Nat Commun*. **7**, 11016 (2016).

72. K. Naydenova, C. J. Russo, Measuring the effects of particle orientation to improve the efficiency of electron cryomicroscopy. *Nat Commun*. **8**, 629 (2017).

73. Y. Z. Tan *et al.*, Addressing preferred specimen orientation in single-particle cryo-EM through tilting. *Nat Meth*. **14**, 793–796 (2017).

74. Y. Liu, R. A. Kahn, J. H. Prestegard, Dynamic structure of membrane-anchored Arf*GTP. *Nat. Struct. Biol.* **17**, 876–881 (2010).

75. K. Shen *et al.*, Architecture of the human GATOR1 and GATOR1-Rag GTPases complexes. *Nature*. **556**, 64–69 (2018).